Monitoring VIIRS Thermal Emissive Bands Long-Term Performance Using Lunar Observations

Yonghong Li[a] and Xiaoxiong Xiong[b]

[a]Science Systems and Applications Inc., 10210 Greenbelt Road, Lanham, MD 20706, USA

[b]Sciences and Exploration Directorate, NASA/GSFC, Greenbelt, MD 20771, USA

ABSTRACT

Two Visible Infrared Imaging Radiometer Suite (VIIRS) instruments are currently operating in space, one onboard the Suomi National Polar-orbiting Partnership (S-NPP) satellite launched on October 28, 2011 and the other onboard the NOAA-20 satellite launched on November 18, 2017. The performance of the seven VIIRS thermal emissive bands (TEBs) is monitored via on-orbit calibration data, the analysis of Earth view observations, as well as inter-comparisons with other sensors. The Moon has been used as a unique invariant target for on-orbit sensor calibration because its surface property is considered extremely stable over time in spectra, radiometry, and geometry with a repeatable lunar phase. This paper presents the assessments of the S-NPP and NOAA-20 VIIRS TEB on-orbit calibration stability using near-monthly scheduled lunar observations over their respective missions. The methodology previously developed for MODIS is now applied to VIIRS to monitor the TEB long-term stability by extracting and trending the lunar brightness temperatures from selected unsaturated pixels. It includes a correction applied to reduce any impact from the Sun–Moon geometry (e.g. Sun-Moon distance variation). The results show that the mission-long brightness temperature trends from the lunar surface are stable for all VIIRS TEBs, despite noticeable seasonal variations in the lunar thermal emissive radiance.

Keywords: VIIRS, calibration, Moon, thermal emissive bands

1. INTRODUCTION

The Visible Infrared Imaging Radiometer Suite (VIIRS), a major instrument with MODIS design heritage for Earth science observations, has been operating onboard the Suomi National Polar-orbiting Partnership (S-NPP) and the NOAA-20 (N20, previously JPSS-1) weather satellites since October 2011 and November 2017, respectively. VIIRS has seven thermal emissive spectral bands. Two of the thermal emissive bands (TEBs) are imaging resolution bands (I-bands, I4 and I5) and the other five TEBs are moderate resolution bands (M-bands, M12–16). The spatial resolutions at nadir are 375 m for the I-bands and 750 m for the M-bands [1]. There are 3 aggregation zones along-scan in the VIIRS Earth view data collection [2].

To maintain the VIIRS TEB data quality for the downsteam science data products, the onboard telemetry temperatures, the calibrator (blackbody) data, as well as the calibration coefficients derived are closely monitored to assess the stability of the on-orbit TEB performances [2-6]. The VIIRS TEB calibration is also evaluated through simultaneous nadir observations of the Earth view data from other sensor's measurements for the accuracy and/or through the Earth view observation over a certain site for the calibration consistency [7-10].

The Moon has been used as a unique invariant target for the on-orbit sensor calibration because its surface property is considered extremely stable over time in spectra, radiometry, and geometry with a repeatable lunar phase [11]. Unlike the Earth view data, the lunar data are not affected by environmental variables (i.e. atmosphere, water vapor, etc.).

Lunar observations have been used in the calibration of the MODIS instruments to derive band-to-band registration offsets, the response versus scan angle, modulation transfer function, electronic crosstalk coefficients, optical leak corrections, and for the radiometric stability assessment of the TEBs [12-20]. These applications have been extended from

the MODIS to the VIIRS instrument calibration for the validation of its reflective solar bands radiometric calibration stability, spatial registration (band-to-band and detector-to-detector), day/night band calibration, evaluation of the TEB performance, and reflective solar bands calibration [21-28].

Since launch, the lunar observations have been regularly performed on a near-monthly basis for S-NPP and N20 VIIRS. This paper presents the VIIRS TEB radiometric stability performance using lunar observation data. Section 2 introduces the methodology and special considerations used to process the VIIRS TEB lunar data for the radiometric assessments. The results and discussions are presented in Section 3. A summary and our future work are provided in Section 4.

2. METHODOLOGY

2.1 VIIRS TEB calibration algorithm

The VIIRS TEBs are located in two different cold focal plane assemblies (CFPAs). Bands I4, M12 and M13 are in the short and mid-wave infrared (SMIR) CFPA with spectral coverages of 3.740 ± 0.190 μm, 3.700 ± 0.090 μm, and 4.050 ± 0.078 μm. Bands I5 and M14-16 are in the long-wave infrared (LWIR) CFPA with spectral ranges of 11.450 ± 0.950 μm, 8.550 ± 0.150 μm, 10.763 ± 0.500 μm, 12.013 ± 0.475 μm, respectively. Figure 1 illustrates the spectral profiles for each TEB. All TEB data are calibrated on-orbit by observing an onboard temperature controlled blackbody (BB) and a deep space view (SV) port.

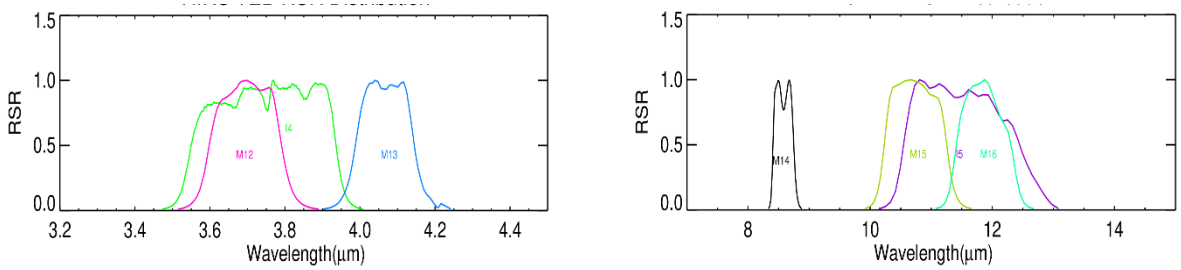

Figure 1 VIIRS TEB spectral coverage. (RSR: relative spectral response)

The VIIRS TEB calibration converts the digital number of a detector response to the sensor's at-aperture radiance. For each scan, the sensor observes the BB and the SV. The BB measurement (dn_{BB}) is then obtained by subtracting the detector response of the SV, which is considered as the instrument background, from the raw detector response of the BB. The BB assembly is designed to provide known radiance levels for the TEB calibration with a close-to-unity emissivity (greater than 0.996) and excellent temperature uniformity [29]. Its radiance can be calculated by

$$L_{total} = RVS_{BB} \cdot L_{BB} + (RVS_{BB} - RVS_{SV}) \cdot \frac{(1-\rho_{RTA})L(T_{RTA}) - L(T_{HAM})}{\rho_{RTA}}, \quad (1)$$

where

$$L_{BB} = \varepsilon \cdot L(T_{BB}) + (1 - \varepsilon) \cdot [w_{RTA} \cdot L(T_{RTA}) + w_{sh} \cdot L(T_{sh}) + w_{cav} \cdot L(T_{cav})]. \quad (2)$$

In Eqs. (1)-(2), *RVS* represents the relative response versus scan-angle. *T* and *L*(*T*) are temperature and the temperature dependent radiance. *RTA*, *cav*, *HAM*, and *sh* represent the rotating telescope assembly, instrument cavity, half angle mirror, and the BB shield, respectively. *w* is the pre-launch determined weight ($w_{RTA} + w_{sh} + w_{cav} = 1$) for these three contribution sources. ρ and ε are the spectral reflectance of the RTA and the BB emissivity. The relationship between dn_{BB} and L_{total} is described by a quadratic model

$$L_{total} = F \cdot (\sum_{i=0}^{2} c_i dn_{BB}^i), \quad (3)$$

where c_i (i = 0, 1, 2), provided via a look-up-table, are temperature dependent calibration coefficients for each band,

detector, and HAM side. *F* is a calibration scaling factor (F-factor). The F-factor is derived from Eq. (3) on a scan-by-scan basis and then applied to the Earth view (EV) data by

$$L_{EV} = \frac{1}{RVS_{EV}}[F \cdot \sum_{i=0}^{2} c_i \cdot dn_{EV}^{i} - (RVS_{SV} - RVS_{EV}) \cdot \frac{L(T_{ham}) - (1-\rho_{RTA}) \cdot L(T_{RTA})}{\rho_{RTA}}]. \quad (4)$$

Currently, the *c* coefficient look-up-tables employed in the on-orbit VIIRS TEB calibration were derived from prelaunch data analyses.

2.2 Lunar observation data acquirement

The VIIRS lunar observations are made during the daytime. These are performed through a spacecraft maneuver so that the lunar image is captured through the SV port. The lunar observations are regularly scheduled on a near-monthly basis when the lunar phase is within a small range (-51.5 to -50.5 degrees). A sector rotation is usually implemented to have lunar data collected in the EV data sector so that the images from all of the spectral bands are co-registered. For the dual gain bands, the detector gains are fixed at high gains during the scheduled lunar observations. There have been 7–9 lunar observations each year since launch.

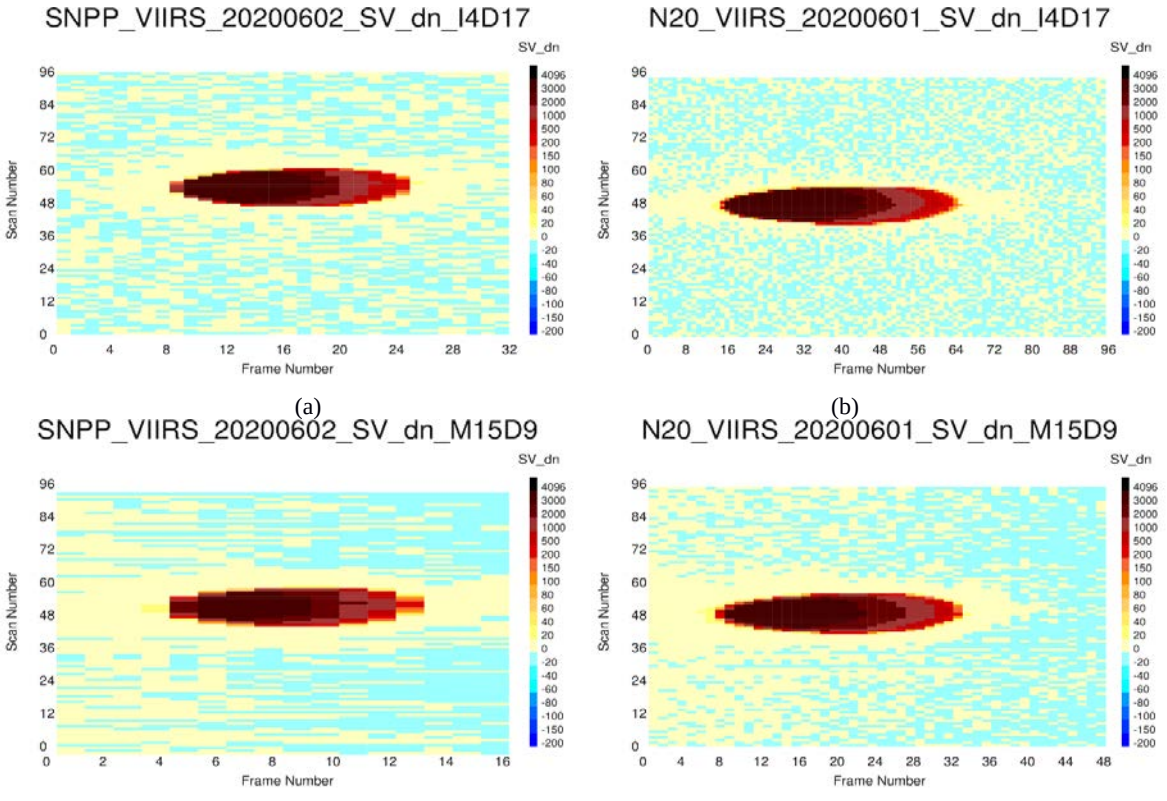

Figure 2 VIIRS lunar observation images for S-NPP (left) on 06/02/2020 and N20 (right) on 06/01/2020. (a) S-NPP band I4 D17; (b) N20 band I4 D17; (c) S-NPP band M15 D9; (d) N20 band M15 D9.

When VIIRS observes the Moon through the SV port, the Moon moves into and out of the field-of-view (FOV) in the along-track direction and is observed in about 30 scans. The orientation of the Moon image in a lunar observation relates to the geometry between the VIIRS sensor and the Moon at the moment. For each lunar observation event, there are less than 10 scans that capture a complete lunar image. The lunar image is typically observed in aggregation zone 3 for S-NPP VIIRS and zone 1 for N20 VIIRS (except for the first lunar event observed in aggregation zone 2).

Figure 2 illustrates the VIIRS lunar observation images from the middle detector of two TEBs (I4 detector (D) 17 and M15 D9) for S-NPP on 06/02/2020 and N20 on 06/01/2020. As seen from the horizontal axis ("Frame Number"), the Moon appears in aggregation zone 3 in S-NPP VIIRS (including 32 frames for the I-band and 16 frames for the M-band) while it is observed in aggregation zone 1 in N20 VIIRS, which contains 96 frames for the I-band and 48 frames for the M-band, respectively.

The detector response acquired from the lunar observation through the SV port are digital number, for which a dark reference needs to be subtracted. The corresponding radiance of the lunar surface is calculated by

$$L_{moon} = F \cdot \sum_{i=0}^{2} c_i \cdot dn_{moon}^{i} , \quad (5)$$

where dn_{moon} is the background corrected lunar response of a detector.

2.3 Considerations of using lunar data for VIIRS TEB calibration assessments

Unlike the reflective solar bands, all of the VIIRS TEBs are partially saturated during the scheduled lunar observations. Therefore, it is crucial to select pixels properly from the lunar image data for the VIIRS TEB calibration assessment.

For each lunar observation event, the lunar image size seen by the VIIRS sensor is determined from the real Moon size, the Moon-sensor (VIIRS) distance, and the sensor altitude. With an assumption that the Moon image is a circular disk, the number of lunar image pixels is then obtained by the lunar image area, sensor spatial resolution at nadir, and the aggregation zone that the lunar image is located.

In this study, seven unsaturated lunar image pixels, starting from the *N*-th largest radiance pixel (including saturation pixels), are selected for the M-band (except M13) for the S-NPP VIIRS TEB calibration assessment. This number is doubled for the I-bands (because of different spatial resolutions) and tripled for band M13 (because its data is not aggregated). For the N20 VIIRS TEBs, the number of unsaturated lunar image pixels is tripled to match the different aggregation zones between the two VIIRS instruments. The threshold (*N*) is *k* percent of the lunar image pixels with an over sampling factor adjustment. *k* is the maximum percentage of saturated pixels in the lunar image disk in all of the TEB detectors for all lunar observations over the entire mission. An additional two percent was added to the *k* value in this study.

The average radiance (*rad*) of the selected pixels was used to trend each TEB. Its corresponding brightness temperatures (BTs) were calculated using Planck function and the center wavelengths of each TEB. To remove the impact from the differences of the Sun-Moon distances ($d_{\text{sun-moon}}$ in astronomical unit) and the lunar phase angles (θ) among the lunar observations, the BTs were corrected by the Sun-Moon distance changes and then were normalized to the lunar phase angle of 51°. Thus, the corrected brightness temperature (hereafter known as BT_{corr}) is

$$BT_{corr} = BT \cdot \sqrt{d_{sun-moon}} \cdot (\theta - 51) \cdot s, \quad (6)$$

where *s* is the change rate of the Sun-Moon distance corrected radiances versus phase angles extracted from all lunar observation data.

3. RESULTS AND DISCUSSIONS

In this study, the VIIRS TEB lunar surface BTs were trended from January 27, 2018 to June 1, 2020 for N20 VIIRS and from April 2, 2012 to June 2, 2020 for S-NPP VIIRS. The calibration parameters (F-factor and c_i), were determined based on the on-orbit BB and telemetry measurements at the same orbits of the lunar events. The time series of the lunar surface BTs presented below are for BT_{corr}.

Figure 3 shows the BT_{corr} trends for MWIR bands I4, M12, and M13. These are stable over the mission lifetime. The BT_{corr} of bands I4 and M12, with nearly the same center wavelengths (see Figure 1), are consistent for both N20 VIIRS and S-NPP VIIRS. Larger variations are observed in the S-NPP VIIRS MWIR TEBs (2.8 K for band I4 and 4.3 K for band M12), while it is only 2.0 K for N20 bands I4 and M12. The S-NPP band M12 detector 16 behaves slightly out-of-family. The BT_{corr} of band M12 are higher than those of band M13 for the two VIIRS instruments. The BT_{corr} values of the N20 VIIRS MWIR bands are lower than S-NPP VIIRS's because there are more saturated pixels in the N20

TEBs during the lunar observations. The band averaged BT_{corr} and the average variation ranges are detailed in Table 1.

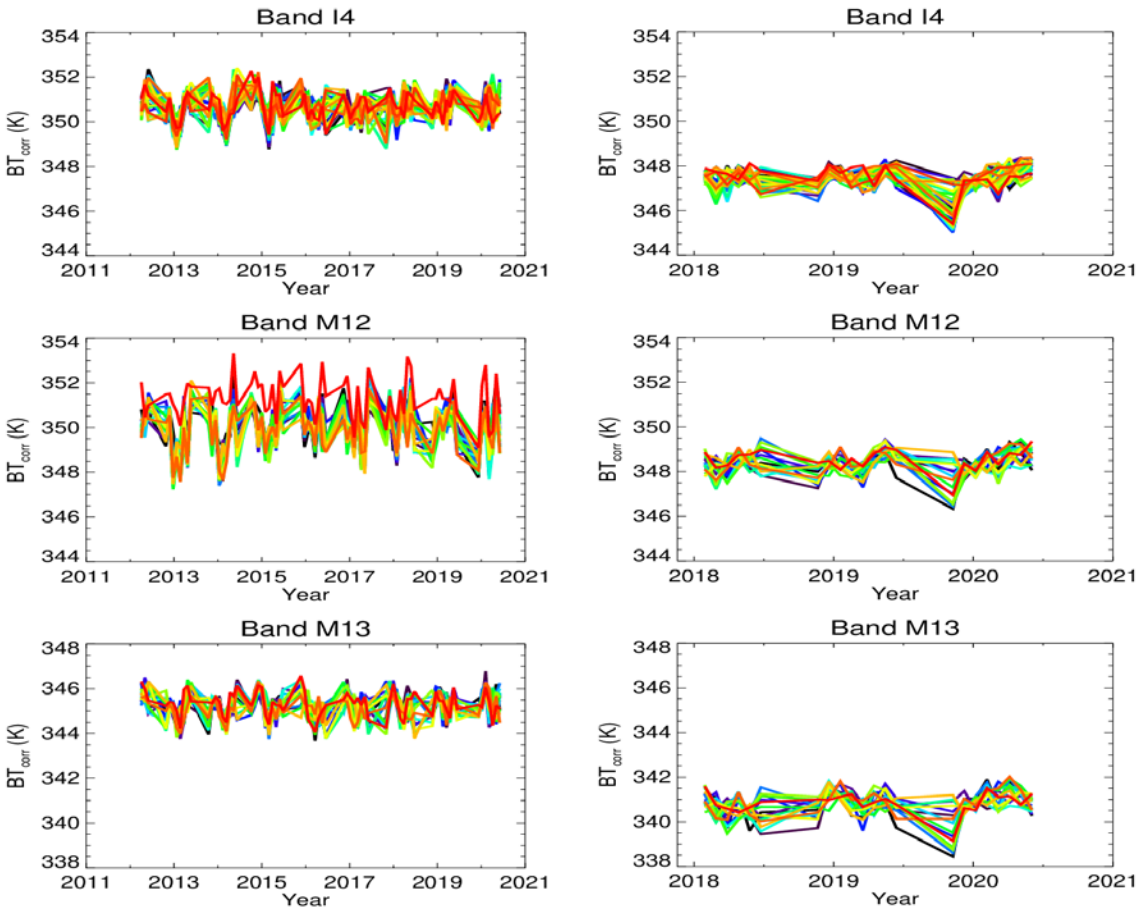

Figure 3 Time series of the BT_{corr} for VIIRS MWIR bands I4, M12, and M13 from scheduled lunar observations. (a) S-NPP; (b) N20.

Table 1 Band averaged BT_{corr} and their variation ranges. (unit: K)

Band	S-NPP		N20	
	Mean	Var. Range	Mean	Var. Range
I4	350.7	2.8	347.5	2.0
I5	337.9	5.0	333.3	3.7
M12	350.1	4.3	348.4	2.0
M13	345.3	2.4	340.8	2.3
M14	338.7	6.6	336.1	3.1
M15	337.0	8.0	332.8	3.6
M16	337.0	8.4	331.4	3.8

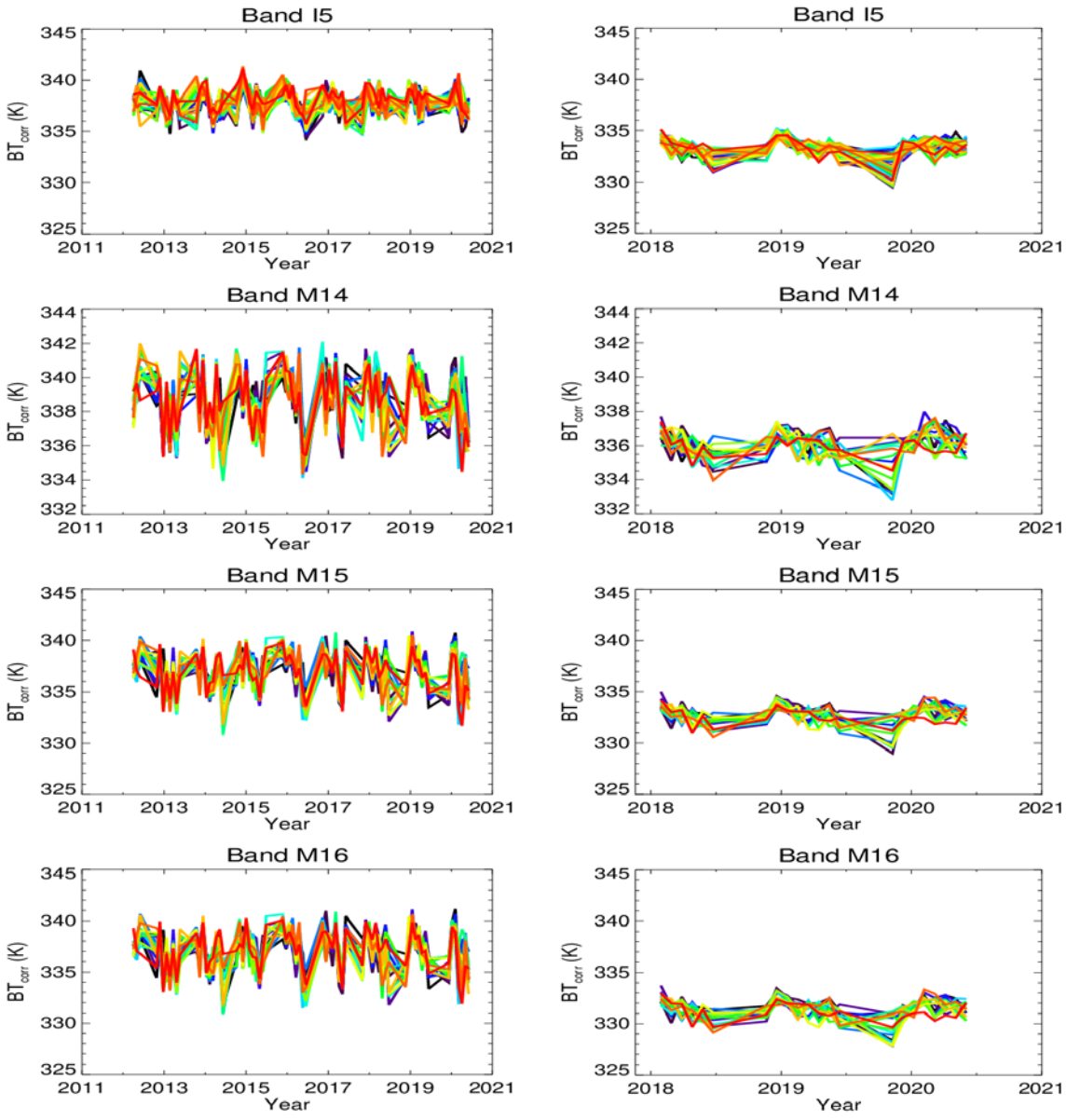

Figure 4 Time series of the BT_{corr} for VIIRS LWIR bands I5 and M14-16 from scheduled lunar observations. (a) S-NPP; (b) N20.

Figure 4 illustrates the BT_{corr} trends for LWIR bands I5 and M14-16. No out-of-family detector is observed, and the trends are stable over both missions for all of the LWIR bands. The band averaged BT_{corr} measured by bands I5, M15, and M16, which have spectral overlaps (see Figure 1), agree well within 1 K for S-NPP VIIRS. For N20 VIIRS, the difference of the band averaged BT_{corr} between bands I5 and M15 is about 0.5 K. The band averaged BT_{corr} of band M15 is higher than that of band M16 by about 1.4 K. The BT_{corr} of band I5 is larger than bands M15 and M16 for both VIIRS instruments. Bands M15 and M16 have larger fluctuations in the BT_{corr} time series than band I5 for S-NPP

VIIRS, while the variation range of those bands are similar for N20 VIIRS. The average BT_{corr} change ranges of the N20 VIIRS LWIR M-bands are only half of their corresponding S-NPP VIIRS bands. Overall, the BT_{corr} of the LWIR bands are lower than those of the MWIR bands (see Table 1). Similar to the MWIR bands, the BT_{corr} values of the LWIR bands obtained from N20 VIIRS are relatively lower than those from S-NPP VIIRS because more pixels in the N20 are saturated during the lunar observations.

The lunar surface brightness temperature trends in Figures 3-4 indicate that the VIIRS TEBs are well calibrated and stable for both missions (S-NPP and N20). It also provides evidence that the two VIIRS instruments work well for scenes with higher BTs.

For VIIRS TEB calibration assessments using lunar observation data, the unsaturated lunar image pixels can be selected from the top radiance pixels, which has been detailed in this study. The assessment is limited by the selection of the unsaturated lunar image pixels, which ideally should be at the same locations on the Moon image disk for all lunar observation events.

4. SUMMARY AND FUTURE WORK

The assessments of the S-NPP and N20 VIIRS TEB on-orbit calibration stability are conducted using near-monthly scheduled lunar observations. The Moon has been used as a unique invariant target for on-orbit sensor calibrations because its surface properties are stable, both spatially and radiometrically, and the lunar phase is repeatable. The results show that the mission-long trends of the BTs from the lunar surface (with much higher BTs than the onboard BB) are stable for all VIIRS TEBs, both S-NPP and N20. The variation ranges of the lunar surface brightness temperatures from the LWIR bands (I5 and M14-16) are relatively larger than those from the MWIR bands (I4, M12, and M13). More fluctuations are observed in the S-NPP VIIRS TEBs. In order to better evaluate the consistency of the lunar brightness temperature measurements between the N20 and S-NPP VIIRS TEBs, further investigations will be explored to make the two measurements comparable.

ACKNOWLEDGEMENTS

The authors would like to thank other members of the NASA VIIRS Characterization Support Team (VCST) and NOAA VIIRS SDR Team for their technical support on the VIIRS instrument operation and calibration. The authors would also like to thank Zhipeng Wang for his previous work on this topic and Amit Angal for providing the lunar raw data, as well as Aisheng Wu and Carlos Perez-Diaz for their comments and suggestions in preparing the manuscript.

REFERENCES

[1] Schueler C., Clement J.E., Ardanuy P., Welsh C., DeLuccia F., and Swenson H., "NPOESS VIIRS sensor design overview," Proc. SPIE 4483 (2002).

[2] Cao C., Xiong X., Blonski S., Liu Q., Uprety S., Shao X., Bai Y., and Weng F., "Suomi NPP VIIRS sensor data record verification, validation, and long-term performance monitoring," Journal of Geophysical Research: Atmospheres, 118, 11664–11678, (2013).

[3] Cao C., De Luccia F.J., Xiong X., Wolfe R., and Weng F., "Early on-orbit performance of the visible infrared imaging radiometer suite onboard the Suomi National Polar-Orbiting Partnership (S-NPP) Satellite," IEEE Trans. on Geoscience and Remote Sensing ,52(2), 1142–115 (2014).

[4] Cao C., Blonski S., Wang W., Uprety S., Shao X., Choi J., Lynch E., and Kalluri S., "NOAA-20 VIIRS on-orbit performance, data quality, and operational Cal/Val support," Proc. SPIE, 10781,107810K(2018).

[5] Efremova B., McIntire J., Moyer D., Wu A., and Xiong X., "S-NPP VIIRS thermal emissive bands on-orbit calibration and performance," J. Geophys. Res. Atmos., 119, 10,859–10,875 (2014).

[6] Li Y., Xiong X., McIntire J., Angal A., Gusev S., and Chiang K., "Early Calibration and Performance Assessments of NOAA-20 VIIRS Thermal Emissive Bands," IEEE Trans. on Geoscience and Remote Sensing, 57(11), 9242–9251 (2019).

[7] Efremova B., Wu A., and Xiong X., "Relative spectral response corrected calibration inter-comparison of S-NPP VIIRS and Aqua MODIS thermal calibration inter-comparison of S-NPP VIIRS and Aqua MODIS thermal emissive bands," Proc. SPIE 9218, 92180G (2014).

[8] Moeller C., Moyer D., Tobin D., Quinn G., Cao C., Liu M., Padula F., and Wang W., "S-NPP VIIRS thermal emissive band (TEB) validation update," SuomiNPP SDR Science and Products Review, College Park, MD, USA. (2013). [Online] Available: https://www.star.nesdis.noaa.gov/star/documents/meetings/S-NPPSDR2013/dayTwo/Moeller_VIIRS.pdf

[9] Li Y., Xiong X., McIntire J., and Wu A., "Comparison of the MODIS and VIIRS Thermal Emissive Band Radiometric Calibration," IEEE Trans. on Geoscience and Remote Sensing, 58(7), 4852–4859 (2020).

[10] Madhavan S., Brinkmann J., Wenny B., Wu A., and Xiong X., "Evaluation of VIIRS and MODIS thermal emissive band calibration stability using ground target," Remote Sensing, 8(2), 158 (2016).

[11] Kieffer, H.H. and Stone, T. C., "The spectral irradiance of the Moon," Astronomical Journal, 129(6), 2887-2901 (2005).

[12] Xiong X., Sun J., Xiong S., and Barnes W., "Using the Moon for MODIS On-orbit Spatial Characterization," Proc. SPIE 5234, 480-487 (2003).

[13] Sun J., Xiong X., Barnes W., and Guether B., "MODIS reflective solar bands on-orbit lunar calibration," IEEE Trans. on Geoscience and Remote Sensing, 45(7), 2383–2393 (2007).

[14] Choi T., Xiong X., and Wang Z., "On-orbit lunar modulation transfer function (MTF) measurements for the moderate resolution imaging spectroradiometer (MODIS)," IEEE Trans. on Geoscience and Remote Sensing, 52(1), 270–277 (2014).

[15] Wang Z., Xiong X., Choi T., and Link D., "On-orbit characterization of MODIS modulation transfer function using the Moon," IEEE Trans. on Geoscience and Remote Sensing, 52(7), 4112–4121 (2014).

[16] Sun J., Xiong X., Madhavan S., and Wenny B., "Terra MODIS band 27 electronic crosstalk effect and its removal," IEEE Trans. on Geoscience and Remote Sensing, 52(3), 1551–1561 (2014).

[17] Wilson T., Wu A., Shrestha A., Geng X., Wang Z., Moeller C., Frey R., and Xiong X., "Development and Implementation of an Electronic Crosstalk Correction for Bands 27–30 in Terra MODIS Collection 6," Remote Sensing, 9, 569 (2017).

[18] Li W., Xiong X., Chiang K., and Toller G., "Evaluation of Terra MODIS PC bands optical leak correction algorithm," Proc. SPIE 5882, pp. 588 219.1–588 219.9 (2005).

[19] Xiong X. and Chen H., "Using lunar observations to assess Terra MODIS thermal emissive bands calibration," Proc. SPIE 7807, 78070I (2010).

[20] Wang Z., Xiong X., Chen H., and Madhavan S., "On-orbit radiometric stability assessment of MODIS thermal emissive bands with lunar observation," Proc. SPIE 8866, 886604 (2013).

[21] Xiong X., Wang Z., Sun J., Angal A., Fulbright J., and Butler J., "MODIS and VIIRS lunar observations and applications," Proc. SPIE 8889, 88890V (2013).

[22] Xiong X., Sun J., Fulbright J., and Wang Z., "Lunar calibration and performance for S-NPP VIIRS reflective solar bands," IEEE Trans. on Geoscience and Remote Sensing. 54(2), 1052–1061 (2016)

[23] Choi T., Shao X., Cao C., and Weng F., "Radiometric Stability Monitoring of the Suomi NPP Visible Infrared Imaging Radiometer Suite (VIIRS) Reflective Solar Bands Using the Moon," Remote Sensing, 8(1), 15 (2016).

[24] Wang Z., Xiong X., and Li Y., "Update of VIIRS On-Orbit Spatial Parameters Characterized With the Moon," IEEE Trans. on Geoscience and Remote Sensing, 53(10), 5486–5494 (2015).

[25] Xiong X., Wilson T., Angal A., and Sun J., "Using the moon and stars for VIIRS day/night band on-orbit calibration," Proc. SPIE 11151, 111511Q (2019).

[26] Qiu S., Shao X., Cao C., and Uprety S., “Feasibility demonstration for calibrating Suomi-National Polar-Orbiting Partnership Visible Infrared Imaging Radiometer Suite day/night band using Dome C and Greenland under moon light,” Journal of Applied Remote Sensing, 10(1), 016024 (2016).

[27] Wang Z., Xiong X., Efremova B, and Chen H., “Using the Moon to evaluate the radiometric calibration performance of S-NPP VIIRS thermal emissive bands,” Proc. SPIE 9218, 92181W (2014).

[28] Choi, T., Shao X., and Cao C., “On-orbit Radiometric Calibration of Suomi NPP VIIRS Reflective Solar Bands using the Moon and Solar Diffuser,” Applied Optics 57 (32): 9533-9542 (2018).

[29] Xiong X., Butler J., Chiang K., Efremova B., Fulbright J., Lei N., McIntire J., Oudrari H., Sun J., Wang Z., and Wu A., “VIIRS on-orbit calibration methodology and performance,” J. Geophys. Res. Atmos., 119(9), 5065–5078 (2014).